Check for updates

Ecological Applications, 31(2), 2021, e02230
© 2020 by the Ecological Society of America

Leaf traits and canopy structure together explain canopy functional diversity: an airborne remote sensing approach

Aaron G. Kamoske,[1,5] Kyla M. Dahlin,[1,2] Shawn P. Serbin,[3] and and Scott C. Stark[4]

[1]*Department of Geography, Environment, & Spatial Sciences, Michigan State University, 673 Auditorium Road #116, East Lansing, Michigan 48824 USA*
[2]*Program in Ecology, Evolutionary Biology, & Behavior, Michigan State University, 103 Giltner Hall, 293 Farm Lane #103, East Lansing, Michigan 48824 USA*
[3]*Environmental and Climate Sciences Department, Brookhaven National Laboratory, 98 Rochester Street, Upton, New York 11973 USA*
[4]*Department of Forestry, Michigan State University, 480 Wilson Road #126, East Lansing, Michigan 48824 USA*

Citation: Kamoske, A. G., K. M. Dahlin, S. P. Serbin, and S. C. Stark. 2021. Leaf traits and canopy structure together explain canopy functional diversity: an airborne remote sensing approach. Ecology 31(2): e02230. 10.1002/eap.2230

Abstract. Plant functional diversity is strongly connected to photosynthetic carbon assimilation in terrestrial ecosystems. However, many of the plant functional traits that regulate photosynthetic capacity, including foliar nitrogen concentration and leaf mass per area, vary significantly between and within plant functional types and vertically through forest canopies, resulting in considerable landscape-scale heterogeneity in three dimensions. Hyperspectral imagery has been used extensively to quantify functional traits across a range of ecosystems but is generally limited to providing information for top of canopy leaves only. On the other hand, lidar data can be used to retrieve the vertical structure of forest canopies. Because these data are rarely collected at the same time, there are unanswered questions about the effect of forest structure on the three -dimensional spatial patterns of functional traits across ecosystems. In the United States, the National Ecological Observatory Network's Airborne Observation Platform (NEON AOP) provides an opportunity to address this structure-function relationship by collecting lidar and hyperspectral data together across a variety of ecoregions. With a fusion of hyperspectral and lidar data from the NEON AOP and field-collected foliar trait data, we assessed the impacts of forest structure on spatial patterns of N. In addition, we examine the influence of abiotic gradients and management regimes on top-of-canopy percent N and total canopy N (i.e., the total amount of N [g/m^2] within a forest canopy) at a NEON site consisting of a mosaic of open longleaf pine and dense broadleaf deciduous forests. Our resulting maps suggest that, in contrast to top of canopy values, total canopy N variation is dampened across this landscape resulting in relatively homogeneous spatial patterns. At the same time, we found that leaf functional diversity and canopy structural diversity showed distinct dendritic patterns related to the spatial distribution of plant functional types.

Key words: airborne lidar; forest canopies; forest structure; functional traits; hyperspectral imagery; landscape ecology.

Introduction

The relationship between forest structure and function is a major focus of ecosystem ecology; however, most studies have focused on measurements within traditional forest plots (Ellsworth and Reich 1993, Parker et al. 2004, Fahey et al. 2015, Pedro et al. 2017, Atkins et al. 2018, Gough et al. 2019). These studies have shown that the integral relationship between structure and function drives important canopy processes such as net photosynthetic carbon assimilation (Niinemets 2007), resource use and efficiency (Hardiman et al. 2013), and woody growth (Stark et al. 2012), as well as critical ecosystem processes such as net primary production (Hardiman et al. 2011, Scheuermann et al. 2018). Since the individual traits that drive this structure–function relationship are not constant in space and instead show significant heterogeneity across landscapes (Chambers et al. 2007, Asner et al. 2014), a core question in ecosystem ecology is, do landscape scale patterns of forest functional traits change when whole plant structure is considered?

In addition to this significant spatial variation, plant functional and structural traits also vary in three-dimensional space due to a host of different long-term abiotic growth conditions, crown position within the canopy and competition for light, as well as within-canopy fluctuating light environments across the full vertical and horizontal extent of the canopy (the "canopy volume";

Manuscript received 12 March 2020; revised 26 May 2020; accepted 16 August 2020. Corresponding Editor: Nancy F. Glenn.
[5] E-mail: kamoskea@msu.edu

Ellsworth and Reich 1993). These differing light and growth environments drive variation of important leaf functional traits including leaf mass per area (LMA, the ratio between leaf dry mass and leaf area) and foliar nitrogen (foliar N; g/m_G^2; where m_G is meter of ground) within the canopy volume (Niinemets 2007, Poorter et al. 2009). Moreover, horizontal and vertical patterns of these traits in growth environments create heterogeneous distributions of leaves in three dimensions causing significant variation in canopy-scale carbon assimilation across plant functional types (Niinemets et al. 2015). This variation can be attributed to differing light environments related to the effects of multiple scattering, within-canopy shading, and the density of plant material above and around a given leaf (Harding et al. 2001, Stark et al. 2012). Resulting tradeoffs between light interception, photosynthetic capacity, and construction costs (e.g., the leaf economics spectrum) lead to broadly predictable variation in photosynthetic strategies across the plant species comprising global terrestrial biomes (Reich et al. 1997, Wright et al. 2004).

At the canopy scale, forest structural traits can be used to describe the architectural properties that define a leaf's growth environment. These traits include leaf area density (LAD, the total leaf area per unit of volume), which characterizes the horizontal and vertical spatial variation of leaf area within a canopy (Weiss et al. 2004), and canopy clumping (a measure of foliage aggregation relative to a random spatial distribution of leaf material within the canopy; Pisek et al. 2018). When combined with information on plant function, structural diversity yields important insights into vegetation growth and carbon cycling (Niinemets 2012); however, both can be challenging to quantify at scales larger than vegetation plot without advanced remote sensing technologies (Asner and Martin 2009).

Remote sensing has played a significant role in understanding the global terrestrial carbon cycle for decades (Tucker and Sellers 1986; Schimel 1995, Running et al. 2004, Schimel et al. 2015), with a more recent focus on the use of hyperspectral imagery and lidar to measure forest function and structure. By utilizing hundreds of narrow spectral bands, airborne passive optical hyperspectral imagery (HSI; also known as imaging spectroscopy) provides detailed two-dimensional (2D) information on the spectral and functional properties of leaves at the top of the canopy (Ollinger et al. 2002, Townsend et al. 2003, Dahlin et al. 2013, Asner et al. 2015, Singh et al. 2015). Lidar is an active remote sensing system that utilizes laser pulses to measure distance, which can then be used to accurately estimate the three-dimensional (3D) and internal structure of forest canopies across a range of plants in different biomes (Stark et al. 2012, Kamoske et al. 2019, Shao et al. 2019, Smith et al. 2019). While passive optical data can also be used to estimate variables related to forest structure, including clumping index (Pisek et al. 2018) and 3D point clouds through structure-from-motion methods (Dandois and Ellis 2013, Iglhaut et al. 2019), the results are not as robust as active methods like lidar for generating 3D plant information. Compared to HSI data, lidar can yield detailed insights into plant architecture but does not provide the information necessary to map leaf functional traits across space and time, a combination of these data sources is required to provide a complete picture of vegetation structural and functional diversity. However, few publicly available opportunities and platforms exist for the simultaneous collections of these two complementary technologies (Kampe et al. 2010, Cook et al. 2013), limiting our ability to combine landscape-scale information about forest structural and functional traits that play critical roles in whole-canopy processes like carbon assimilation.

In this study, we take steps toward addressing the question of how leaf traits and structural heterogeneity determine whole canopy function by considering how spatial patterns of top-of-canopy and total canopy traits vary across a heterogeneous landscape. We detail a reproducible methodology for estimating functional and structural diversity within the canopy volume from airborne lidar and hyperspectral data from the National Ecological Observatory Network's Airborne Observation Platform (NEON AOP; Kampe et al. 2010). We compare the spatial patterns of 3D whole canopy traits derived from our fusion of lidar and hyperspectral data with traditional 2D remote sensing-derived top-of-canopy traits. In addition, we examine the influence of topography, geology, and management regimes on these two measurements of functional diversity at a NEON site consisting of patches of open longleaf pine and dense broadleaf deciduous forests, located in Alabama, USA. These insights could lead to a better understanding of how we scale fine-resolution ecological processes to landscape, continental, and global models (Schimel et al. 2019).

Materials and Methods

Site description

Field measurements and remote sensing data were acquired in Talladega National Forest, Oakmulgee Ranger District (TALL) in west-central Alabama, USA (Fig. 1). TALL is a core NEON site covering 5,300 ha with a mean annual temperature of 17°C and a mean annual precipitation of 1,350 mm. TALL consists of a mosaic of forest types, with higher elevation areas containing an overstory of longleaf pine (*Pinus palustris*) and loblolly pine (*Pinus taeda*), while white oak (*Quercus alba*), Southern red oak (*Quercus falcata*), chestnut oak (*Quercus montana*), blackjack oak (*Quercus marilandica*), mockernut hickory (*Carya tomentosa*), pignut hickory (*Carya glabra*), sweetgum (*Liquidambar styraciflua*), and tulip tree (*Liriodendron tulipifera*) are present in lower elevation bottomlands. TALL is an actively managed site with ongoing logging, restoration, and prescribed burning projects (USDA Forest Service 2005).

FIG. 1. Location of field site. Purple rectangle represents the extent of the aerial data collection of the National Ecological Observatory Network's Airborne Observation Platform (NEON AOP). Inset map shows the extent of the larger map view within the southeastern United States.

Airborne remote sensing data

The NEON AOP collected remotely sensed data from 27 April to 29 April 2018, at TALL. The NEON AOP employs a full-range hyperspectral sensor (380–2,500 nm; 5 nm bands), a high-resolution RGB camera, and a lidar system (Kampe et al. 2010). Flights occurred at an altitude of 1,000 m, resulting in hyperspectral measurements at a 1-m resolution. The lidar system for this collection was a Riegl Q780 Laser Measurement System (Riegl laser measurement systems, Horn, Austria) operated at a scan angle of ±18°, and a beam divergence of 0.8 mRad, resulting in an average point density of 9.48 points/m^2.

Field data collection and lab methodologies

In May 2018, shortly after the AOP collection, we collected leaves from throughout the canopy volume, targeting the dominant species at TALL (10 species total; listed in *Site description*). Foliar samples were collected using a Big Shot line launcher (SherrillTree, Greensboro, North Carolina, USA) and a pole pruner, with each sample's height estimated using a laser range finder and meter marks on the set line. We collected sample locations using a Trimble GEO7x GPS (Trimble, Sunnyvale, California, USA), which were later differentially corrected with Trimble's GPS Pathfinder Office software. As we collected samples from the canopy, they were wrapped in a damp paper towel, sealed in a plastic bag, and placed in a cooler with ice packs. In total, we collected 156 foliar samples from the canopy dominant species (Appendix S1: Fig. S1, Table S1). In addition to leaf samples, we took 120 hemispherical photographs across the site, following the protocol described in Kamoske et al. (2019).

Leaf samples were processed the same day in our mobile laboratory. For each sample (a small branch with multiple leaves) we took three reflectance measurements from different leaves with an SVC HR-1024i Spectroradiometer with an attached LC-RP-Pro leaf clip foreoptic (Spectra Vista Corporation, Poughkeepsie, New York, USA), which collects data from 340 to 2,500 nm with a bandwidth of approximately 2 nm. Leaves from broadleaf samples were placed directly into the leaf clip, while we created mats from needleleaf samples by laying the needles vertically next to one another while taping the ends together. For needleleaf samples, only the needles and not the taped ends were placed into the leaf clip. After each sample, the instrument was recalibrated using a white Spectralon panel. We then collected a minimum of 500 mg of leaf material from the sample using a pair of scissors that were sterilized between each sample. These pieces of leaf material were imaged on a flatbed scanner and processed for area using ImageJ software (Schneider et al. 2012). We placed the leaf material in a paper coin envelope and dried the samples at 70°C for at least 48 h. After drying, we weighed the leaf samples and calculated leaf mass per leaf area (LMA; g/m_L^2, where m_L is meter of leaf material). A subset of these samples (n = 40, ~4 per species) were re-dried, ground to a fine powder using a ball mill (2000 Geno Grinder; Spex Sample Prep, Cridersville, Ohio, USA), with 1.50–2.50 mg weighed in 0.1-mil tin foil vials (AX26DR; Mettler Toledo, Columbus, Ohio, USA), and used to determine the C:N ratio and elemental N content (g N/g leaf, reported as a percentage) employing a CHNS/O elemental analyzer operated in CHN mode, according to the manufacturer's instructions (2400 Series II CHNS/0 Analyzer; Perkin Elmer, Waltham, Massachusetts, USA) at Brookhaven National Laboratory (Upton, New York, USA).

To build a leaf-scale model of percent N to apply to the remaining samples in lieu of determining foliar N in the lab, we used the laboratory-calculated percent N values and the associated mean reflectance values for each wavelength, to train a partial least-squares regression model (PLSR; Serbin et al. 2014, Singh et al. 2015). We withheld 20% of the samples using a weighted random approach, based on the percent N values, as validation data (n = 8) that wasn't used to develop the model and used the remaining samples (n = 32) as model training data. Using a jackknife approach that randomly withholds 20% of the training data through 50 iterations, we calculated a PRESS statistic (up to 15 components) for each iteration. We then selected the number of components for our final model using the lowest PRESS statistic that balanced predictive accuracy between the training and validation data sets. We applied these

equations to the validation data to assess model accuracy. We then applied the final PLSR coefficients to the reflectance measurements of all 156 leaf samples to determine PLSR--derived percent N values. We used the PLSR predicted values in subsequent analysis. This methodology follows the process and code described in Serbin et al. (2014), with all analysis performed in R using the pls package (Mevik and Wehrens 2007).

Lidar methods

Lidar data was processed for LAD (m_L^2/m_G^3, where m_G is meter of ground) at a 10 × 10 m spatial resolution using the canopyLazR package on GitHub (Kamoske et al. 2019). The canopyLazR package uses the methods described by MacArthur and Horn (1969) and is similar to other published methods (Solberg et al. 2006, Sumida et al. 2009, Zhao and Popescu 2009, Stark et al. 2012). By normalizing the point cloud to height above ground, LAD is calculated by counting the number of lidar pulses that enter and exit each voxel in each vertical column of data that has at least one ground return. After removing the bottom 10 m of the canopy due to noise caused by topographic variation (Kamoske et al. 2019), a stack of rasters containing LAD estimates for each 1-m slice of the canopy above this threshold is returned (mean canopy height at TALL is 25 m). LAI is then calculated by taking the sum of LAD values within a given column of voxels within the canopy. While the TALL lidar data set has a considerably higher point density than the NEON lidar data used in Kamoske et al (2019), here we elected to keep this relatively conservative approach to aggregating and filtering these data as these lidar point clouds were processed as part of a larger study where we wanted to maintain data uniformity across sites. Moreover, topographic issues have been shown to be common when using lidar data for DEM generation (Bater and Coops 2009), which are further amplified when using low-density lidar data. To calibrate the lidar-derived LAI estimates to field-collected data, we processed field-collected hemispherical photographs for LAI using the DHP software (Leblanc et al. 2005). We then calculated the slope of a regression equation between these measurements and the lidar-derived LAI estimates (Appendix S1: Fig. S6; Richardson et al. 2009, Sabol et al. 2014). This slope is used as an extinction coefficient in the Beer-Lambert portion of the LAD equation described in Kamoske et al. (2019) and in Appendix S1: Fig. S6. For TALL, we used an extinction coefficient of 0.4982. Here we opted to use a single extinction coefficient for the entire site, rather than separate coefficients for broadleaf, needleleaf, and mixed-species pixels due to difficulties in detecting species differences with lidar data.

Based on our previous work in Kamoske et al. (2019), we then applied a canopy height and LAI mask to each processed LAD raster to minimize noise in the lidar data set. Using Tukey's outlier test (k = 1.5), we removed all outliers from the upper end of the data set, which resulted in all pixels with a canopy height greater than 44 m being removed as well as all pixels with a LAI value greater than 6 (0.002% of pixels). While a LAI value of 6 is a statistical output, it is also greater than our highest field-collected plot-scale LAI value of 4.35. We also removed all pixels with a LAI value equal to 0. Using these masked LAD tiles, we calculated 26 lidar--derived forest structural attributes in raster format at a 10 × 10 m resolution. These include filled canopy volume, canopy porosity, and canopy distribution metrics described in Hardiman et al. (2013), top-of-canopy rugosity, and canopy euphotic, oligophotic, and empty zone metrics described in Lefsky et al. (1999), canopy height metrics described in Shi et al. (2018), and within-canopy rugosity described in Hardiman et al. (2011). All code to calculate these metrics is provided in the canopyLazR package on our GitHub page (see Data Availability). An overall diagram of our workflow is shown in Fig. 2.

Hyperspectral imagery methods

methods

We processed the atmospherically corrected HSI reflectance data before analysis. First, we removed all flight lines from 27 April due to cloudiness, as well as the horizontal (east-west) flight lines from 29 April and 30 April. The remaining north-south flight lines covered the entire TALL site (29 April and 30 April flights covered the same area as the 27 April flights). Next, we visually identified noisy bands in the data set and removed all bands that were below 500 nm, between 1,350 and 1,450 nm, between 1,800 and 2,000 nm, and all bands above 2,400 nm. We then calculated a narrowband NDVI mask (red, 674 nm; NIR, 830 nm; NDVI >0.5) to remove all non-vegetated pixels from further analysis (Dahlin et al. 2014). We used this relatively high NDVI value of 0.5 in order to leave only healthy green vegetated pixels during the subsequent corrections and analysis. We also calculated a brightness mask to remove all shaded pixels using Tukey's outlier test (k = 1.5), where all pixels that have a reflectance below this cutoff at 800 nm are considered outliers and removed. This is a modified version of the methodologies presented by Clark et al. (2005) and Gougeon (1995), which removes all pixels that are less than the mean reflectance value at 800 nm. Following this, we applied a topographic correction to reduce the effects of terrain, view, and illumination on the reflectance data by normalizing the sunlit area within a pixel without changing the sun and sensor positions or the orientation, geometry, and structure of the canopy while also accounting for diffuse radiation (Soenen et al. 2005). Last, we applied a bidirectional reflectance distribution function effects correction (BRDF) with a thick Ross kernel and a dense Li kernel to remove the anisotropic scattering properties of vegetation that

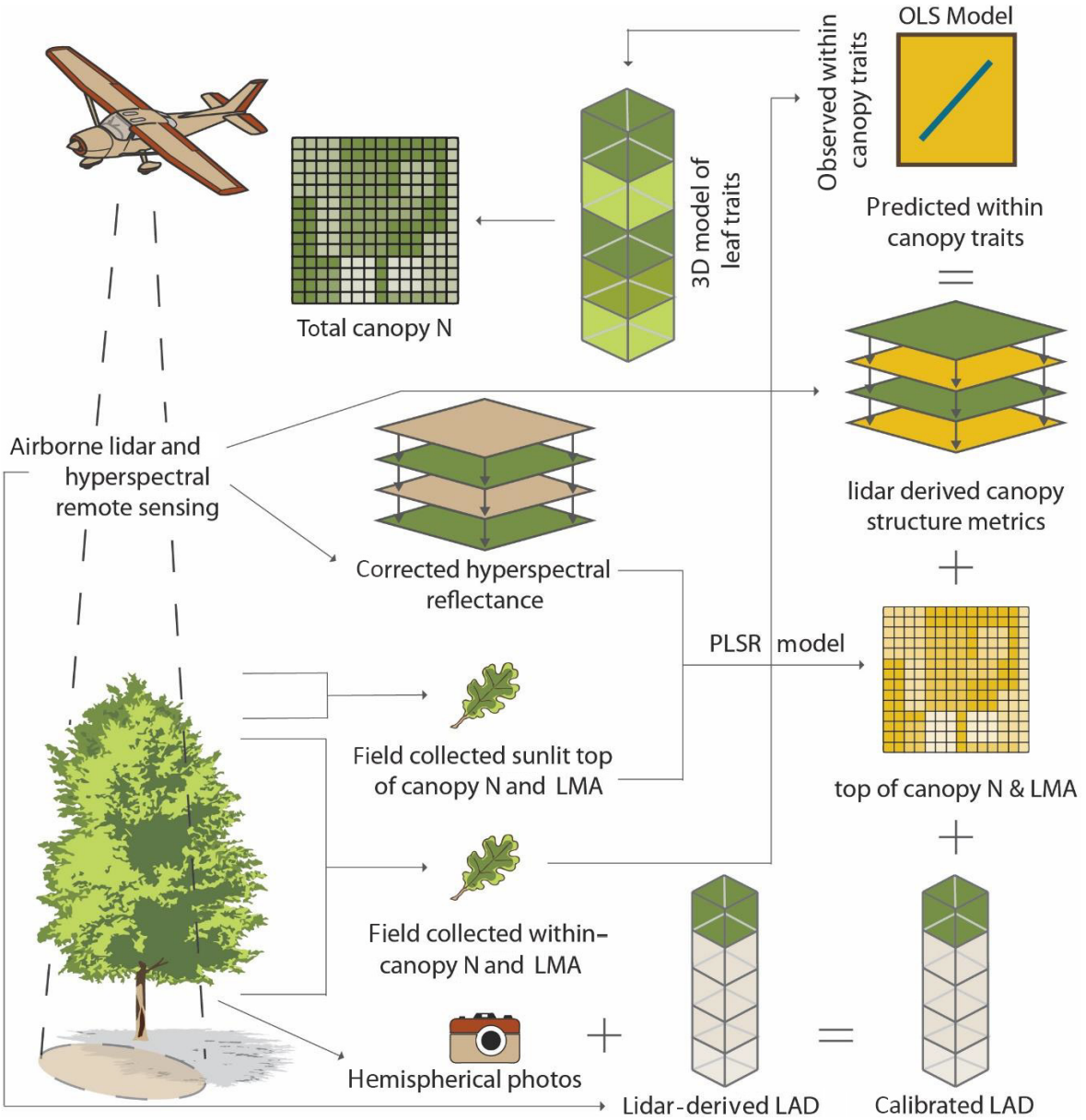

FIG. 2. Workflow diagram showing our methodology for within-canopy trait modeling. LAD, leaf area density (m_L^2/m_G^2, m_L^2 refers to square meters of leaf material, while m_G^2 refers to square meters of ground); LMA, leaf mass per area (g/m_L^2); N, foliar nitrogen content (g N/g leaf); total canopy N, total canopy nitrogen content (g/m^2). Field-collected sunlit top-of-canopy percent N and LMA refers to leaf samples that were collected at the top of the canopy, were constantly sunlit, and had no leaves above (i.e., no sun impediment). Field-collected within-canopy percent N and LMA refer to leaf samples that were collected within the canopy (i.e., not constantly sunlit, shaded, and with other leaves surrounding them).

result in flight line artifacts (Wanner et al. 1995, Collings et al. 2010, Colgan et al. 2012, Schlapfer et al. 2015, Weyermann et al. 2015). Annotated R code to apply these corrections is available on our GitHub page as the hypRspec package (see Data Availability).

From the resulting images, we extracted reflectance data for all top-of-canopy field samples. Due to potential image orthorectification errors, GPS uncertainty, and field challenges, we visually assessed GPS point locations and, when necessary, moved the GPS locations, by hand, 1–2 m to the most appropriate pixel based on a canopy height model and pixel brightness. Due to flight line overlap, many samples had multiple reflectance values. In these cases, we kept the reflectance data from whichever image produced the brightest total reflectance across all bands. We choose to take the brightest reflectance value rather than the median here, in order to filter pixels that were possibly affected by

collection issues related to adverse weather conditions that would not be resolved during the topographic and BRDF correction process.

Once reflectance spectra for all top-of-canopy samples (n = 52) were extracted, we developed PLSR models for top-of-canopy percent N and LMA (Ollinger et al. 2002, Townsend et al. 2003, Singh et al. 2015) using the same methodology and code described for the laboratory data. For the LMA model, we removed all lab measured LMA values that were greater than 259 g/m^2 based on the results from a Tukey's extreme outlier test (k = 3). This outlier test removed six samples from the data set. We removed these outliers from the data set prior to fitting our models, due to PLSR being sensitive to outliers during the calibration and validation process (Martens and Martens 2000). Once PLSR coefficients were calculated for top-of-canopy LMA and percent N, we applied them to the corrected HSI data, resulting in a 1 × 1 m raster for each trait (percent N and LMA). We then filtered the trait maps to remove all extreme outlier pixels (k = 3) and values less than 0 from each 1 × 1 m raster that result from the errors associated with reflectance values collected during image collection. This resulted in 0.09% of the pixels being removed from the final raster. Next, we resampled the mosaicked image to a 10 × 10 m spatial resolution using the mean value within a given kernel, to match the spatial resolution of the lidar-derived rasters. Following this, we mosaicked the flight line rasters together with the mean of overlapping pixels used in the final raster. All analysis was performed in the R programming language and is available on our GitHub page as the hypRspec package (see Data Availability).

Remote-sensing fusion: total canopy N

To model within-canopy LMA, we extracted data from the 26 previously calculated lidar structural attribute rasters, and top-of-canopy percent N and LMA rasters, for all 156 field-sample locations. We also included the height and depth (e.g., distance from the top-of-canopy) for each of the samples in the model. We then removed all top-of-canopy samples (n = 52) since these were used in previous steps and were predicted using the HSI data and PLSR. We then tested the correlation (Pearson's R) between each variable and within-canopy LMA. To avoid multicollinearity, variables with correlations greater than 0.5 to each other were considered too correlated and the predictor most correlated with LMA was kept for further analysis. We then split the data set into validation data (20%; n = 20) and training data (80%; n = 84) using a weighted approach based on species sample counts. Using the previously determined variables we developed an ordinary least squares (OLS) regression model from the training data. To determine the best combination of variables for our final model predicting within-canopy LMA, we used backward stepwise AIC model selection (Burnham et al. 2011, Mascaro et al. 2011). We then applied the resulting coefficients to the validation data set to examine the overall predictive accuracy of our model. Because we did not see a substantial variation of within-canopy percent N in our data (Appendix S1: Fig. S1) or in the literature (Serbin et al. 2014, Bachofen et al. 2020), we used top-of-canopy percent N values for our within-canopy percent N values in lieu of creating another predictive model.

We then applied the final model coefficients to the raster data to create a three-dimensional model of within-canopy LMA (g/m$_L^2$), with any value less than zero set to NA (due to predictive inaccuracy and noise in the raster data). Last, we used these three-dimensional models to calculate within-canopy N per meter of ground area (g/m$_G^2$) using the following equation:

$$N_{tot} = \sum_{i=10}^{h} N_{TOC} \times LMA_i \times LAD_i$$

where N_{tot} is the total canopy N (g/m$_G^2$) for each 10 × 10 m pixel, i refers to each 1-m layer of the canopy, starting at 10 m (layers below 10 m were not considered in this analysis), h is the maximum height of each column of voxels, N_{TOC} is the top-of-canopy N (%), LMA_i is the LMA at each voxel i (g/m$_L^2$) and LAD_i is the LAD at each voxel i. This resulted in a two-dimensional raster for the entire AOP collection area that summarizes functional and structural traits within the canopy volume. We also calculated foliar biomass using the same equation described above but withholding the N_{TOC} values. Last, we removed all extreme outliers from the raster images using Tukey's outlier test (k = 3). All analysis was performed in the R programming language.

Raster differences across scales

To test whether the distinction between leaf-level and canopy traits was scale dependent, we tested the differences between the top-of-canopy and total canopy N rasters at multiple spatial grains. First, we scaled the original 10 × 10 m data to 30 × 30 and 250 × 250 m resolutions to match Landsat and MODIS pixels using the raster package in R (Hijmans 2019). Next, we randomly extracted 10,000 points from the 10 × 10 m and 30 × 30 m rasters and 1,000 points from the 250 × 250 m raster. We then used a linear regression to test the correlations between the two rasters at each spatial resolution. To compare the spatial patterns of the two rasters, we scaled and centered the rasters using the scale function in the raster package and then subtracted the normalized total canopy N raster from the normalized top-of-canopy percent N raster.

To compare the overall spatial patterns of the two maps, we extracted 10,000 random points from the top-of-canopy and total canopy rasters at the 10 × 10 m resolution and fit variograms to these samples. We compared estimates of spatial autocorrelation as well as differences in the nugget, sill, and range of the variograms.

Environmental driver analysis

To understand the influence of abiotic gradients and management practices on the spatial patterns of top-of-canopy percent N and total canopy N (g/m_G^2), we assessed and analyzed the spatial patterns of the data, using multiple regression and Moran's I to test these relationships.

To quantify the abiotic gradients and management practices, we calculated 26 topographic, geologic, and management variables using ArcGIS, QGIS, and R (Appendix S1: Table S2). Topographic variables were calculated from the 10 × 10 m lidar data, geologic variables were downloaded from the USGS (Horton et al. 2017), and management variables were downloaded from the U.S. Forest Service (available online).[2] All variables were transformed into rasters for subsequent analysis.

We performed a Monte Carlo test with 1,000 simulations to calculate a distribution of model coefficients, Moran's I of the residuals, and R^2. During each simulation, we extracted 10,000 random points from the rasters. We then standardized all non-binary variables (Gelman 2007; mean = 0, standard deviation = 0.5) to allow direct comparison between model coefficients. We developed two regression models, one for top-of-canopy percent N and one for total canopy N (g/m_G^2). For each simulation and for each regression model, we used the following methodology. First, we tested the correlation between each variable (Pearson's R) to avoid multicollinearity, with correlations greater than 0.5 considered to be too correlated and the predictor most correlated with N kept for further analysis. Using the remaining variables, we developed an OLS regression equation. With these results, we used backward stepwise AIC model selection to determine the best combination of variables for each of our final models. Any remaining variables with non-significant coefficients ($P > 0.05$) were then removed. We then used these variables in a final OLS regression. To test for spatial autocorrelation, we calculated Moran's I on the model residuals. All analysis was performed with the R programming language.

Results

Trait prediction with PLSR: from leaf to canopy

To predict leaf-level percent N, we used a PLSR model with five components to produce the best results between training and validation data (Table 1; Appendix S1: Fig. S2). This model had an R^2 of 0.90 for the training data, an R^2 of 0.78 for the validation data, and an R^2 of 0.87 when applied to all the data. All models had $P < 0.001$. Across the lab-measured percent N samples, values ranged from 0.55% to 2.64% and PLSR-predicted values ranged from 0.40% to 2.64%. For subsequent steps, we used PLSR-predicted values.

[2] https://data.fs.usda.gov/geodata/edw/datasets.php

Table 1. R^2 from partial least-squares regression (PLSR) models.

	Data set		
Model	Training	Validation	All
Lab percent N PLSR	0.9	0.78	0.87
HSI percent N PLSR	0.61	0.57	0.56
HSI LMA PLSR	0.72	0.77	0.73

Notes: HSI, hyperspectral imagery. All models have $P < 0.001$.

To predict the top-of-canopy percent N from the HSI data, we used a PLSR model with five components. This model had an R^2 of 0.61 for the training data, an R^2 of 0.57 for the validation data, and an R^2 of 0.56 when applied to all the data (Table 1; Appendix S1: Fig. S3). All models had $P < 0.001$. After applying the PLSR coefficients across the images and removing extreme outliers using a Tukey's outlier test ($k = 3$), percent N values ranged from 0.004% to 3.048% (Fig. 3a), which is comparable to the ranges of percent N found in eastern United States temperate forests by Serbin et al. (2014).

To predict LMA from the HSI data, we used a PLSR model with eight components. This model had an R^2 of 0.72 for the training data, an R^2 of 0.77 for the validation data, and an R^2 of 0.73 when applied to all the data (Table 1; Appendix S1: Fig. S4). All models had $P < 0.001$. Across the field-measured samples, LMA values ranged from 20.72 to 326.02 g/m_L^2. After applying the PLSR coefficients to the images and removing extreme outliers using a Tukey's outlier test ($k = 3$), LMA values ranged from 0.041 to 356.7 g/m_L^2 (Fig. 3b). While these values are extrapolated outside of the range of values used in our PLSR model, they are comparable to LMA ranges found globally by Poorter et al. (2009).

Within-canopy leaf traits: Lidar and HSI

To predict within-canopy LMA, our final model consists of four lidar-derived metrics. These metrics included top-of-canopy percent N, sample height, euphotic zone depth, and standard deviation of LAD within a column of voxels. Our final model for within-canopy LMA had an R^2 of 0.51 for the training data and an R^2 of 0.50 for our validation data (Appendix S1: Fig. S5). Both models had $P < 0.001$.

After summing all within-canopy values we calculated the total amount of N (g/m_G^2; Fig. 4), foliar biomass (g/m_G^2; Fig. 3d), and LAI (m_L^2/m_G^2; Fig. 3c) for each pixel. We then removed extreme outliers using Tukey's outlier test ($k = 3$). Values greater than 15 g/m_G^2 were removed from the total canopy N raster (0.03% of raster pixels), values greater than 2,465 g/m_G^2 were removed from the foliar biomass raster (0.46% of raster pixels),

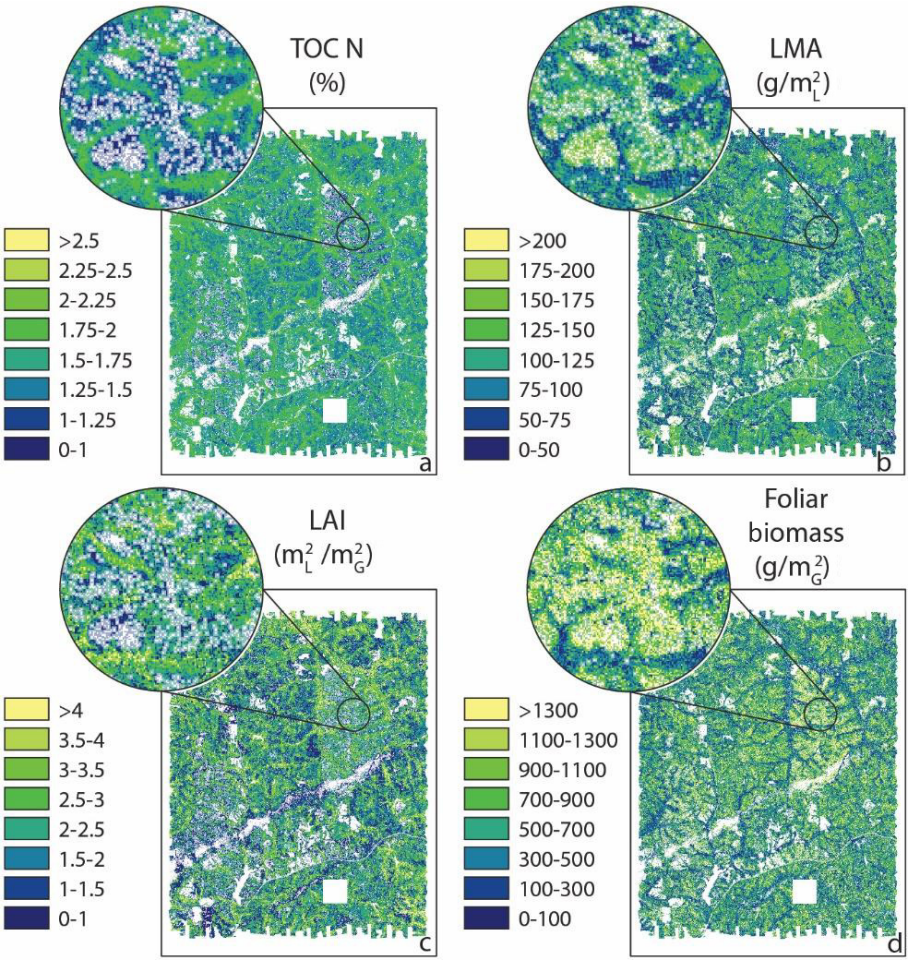

FIG. 3. Maps of functional and structural traits derived from NEON AOP hyperspectral imagery (his) and lidar data showing (a) top of canopy N, (b) LMA, (c) LAI, and (d) foliar biomass. TOC, top-of-canopy; m_L^2 refers to square meters of leaf material, while m_G^2 refers to square meters of ground. Call-out circle is a 1 km radius around the NEON flux tower at this site, shown as a star.

and values greater that 7 m_L^2/m_G^2 were removed from the LAI raster (0.03% of raster pixels).

To illustrate the differences in canopy profiles of within-canopy N (g/m_G^3) we extracted data from the total canopy rasters using the GPS locations of a white oak (Fig. 4a) and longleaf pine (Fig. 4b) sample from our field data. The total amount of N in the white oak sample was 6.99 g/m_G^2 while there was 7.93 g/m_G^2 in the canopy of the longleaf pine sample. Moreover, the profiles of each sample illustrate differing within-canopy allocation strategies for the two species.

Top-of-canopy and total canopy N: differing spatial patterns

After normalizing (mean = 0, SD = 1) the top-of-canopy percent N and total canopy N (g/m_G^2) rasters for equal comparison, there was no relationship between the two variables at any of the spatial resolutions, showing that these differences are not scale dependent (Fig. 5, panels a–c). Prior to normalization, we used linear regression to test the relationship between the two variables at each spatial resolution (Fig. 5, panels d–f). All linear regressions were significant ($P < 0.05$), but the largest R^2 value was 0.02, showing a very weak relationship between top-of-canopy and total canopy N across spatial resolutions. This lack of relationship shows that as data is aggregated together at coarser spatial resolutions, resulting in pixels containing multiple PFTs rather than single species, there are still distinct differences between top-of-canopy and total canopy N.

To assess differences in spatial patterns across the landscape, we calculated variograms for the top-of-canopy percent N and total canopy N (g/m_G^2) data sets (Fig. 6). A comparison of Moran's I values for the two normalized (mean = 0, SD = 1) data sets showed that the top-of-canopy percent N map was substantially more spatially autocorrelated (Moran's $I = 0.026$) than the total canopy N map (Moran's $I = 0.014$). For the non-normalized data sets, top-of-canopy percent N

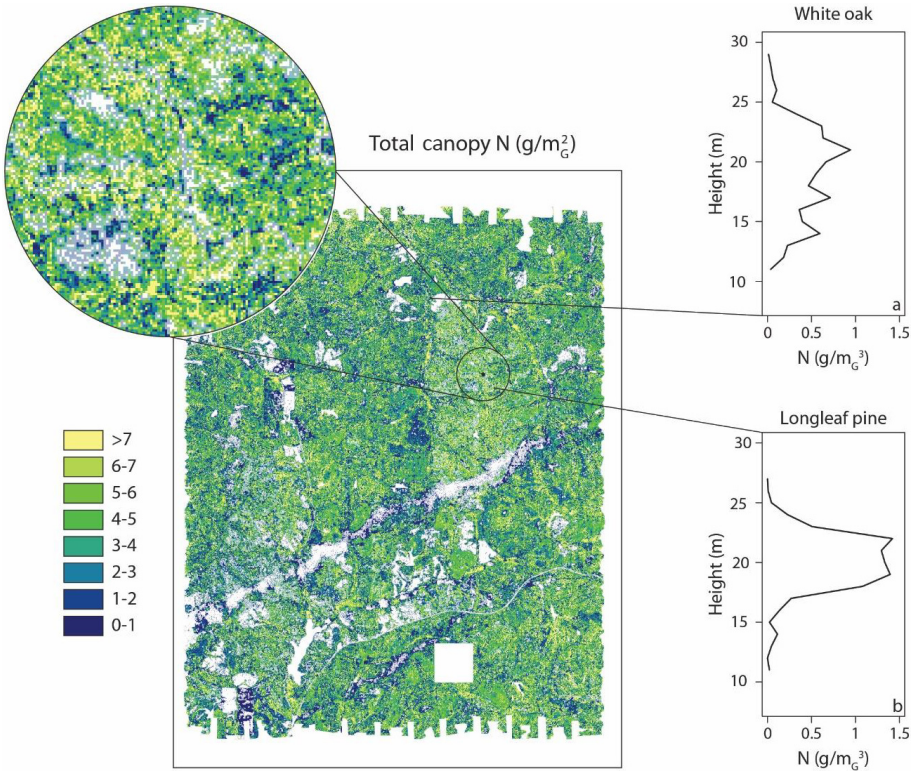

FIG. 4. Map of total canopy N (g/m$_G^2$) and within-canopy N (g/m$_G^3$) profiles from white oak (total foliar N = 6.99 g/m$_G^2$) and longleaf pine (total foliar N = 7.93 g/m$_G^2$). Locations were extracted based on the GPS positions of field samples. Call out circle is a 1 km radius around the NEON flux tower at this site, show as a star.

samples exhibit spatial autocorrelation up to a distance of 1,200 m, while total canopy N (g/m$_G^2$) samples are spatially autocorrelated up to a distance of 700 m. Partial sill (Psill) measurements also differ substantially, showing differences in variability between pairs of points, with top-of-canopy percent N having a value of 0.23 and total canopy N (g/m$_G^2$) having a value of 0.09. The shapes of the variograms indicate that top-of-canopy percent N is grouped into clusters of similar values (lower nugget, longer range), while the total canopy N values are more evenly distributed (higher nugget, shorter range).

Regional patterns and environmental drivers: assessing spatial structure

Elevation visually appeared to be a strong driver of leaf trait spatial distributions in our maps (Fig. 3). To quantify this relationship, we looked at the influence of elevation on top-of-canopy percent N, total canopy N (g/m$_G^2$), and the normalized difference between these two data sets (Fig. 7). Top-of-canopy percent N was related to elevation (R^2 = 0.13), while total canopy N (g/m$_G^2$) was not related to elevation (P > 0.05). Therefore, the correlation between the normalized difference of these two estimates and elevation (R^2 = 0.06) is mostly due to the stronger correlation between elevation and top-of-canopy percent N.

To more broadly understand the effects of abiotic gradients and management regimes on leaf and canopy functional traits, we performed a Monte Carlo simulation on the abiotic and management rasters to compile a distribution of results. Models predicting top-of-canopy percent N had a mean R^2 of 0.24 with a standard deviation of 0.009. Eleven of the predictors appeared in over 20% of the models (Fig. 8), seven variables appeared in no models, and seven variables appeared in all the models (Table 2). The only major topographic predictor (coefficient > 0.1) with a positive coefficient was soil wetness index (SWI), while major topographic predictors with a negative coefficient included elevation (DTM), solar radiation at the winter solstice (SR.WS), and TPI (topographic position index). The only major geologic predictor (coefficient > 0.1) with a negative coefficient was Coker substrate, while Eutaw substrate had a positive coefficient and was a major geologic predictor. The only major management variable (coefficient > 0.1) was areas burned in 2018 and it had a negative coefficient.

Total canopy N (g/m$_G^2$) models had a mean R^2 of 0.03 with a standard deviation of 0.003. Eleven of the predictors appeared in over 20% of the models (Fig. 8), four variables appeared in no models and two variables appeared in all the models (Table 2). Solar radiation at the summer solstice was the only major topographic predictor

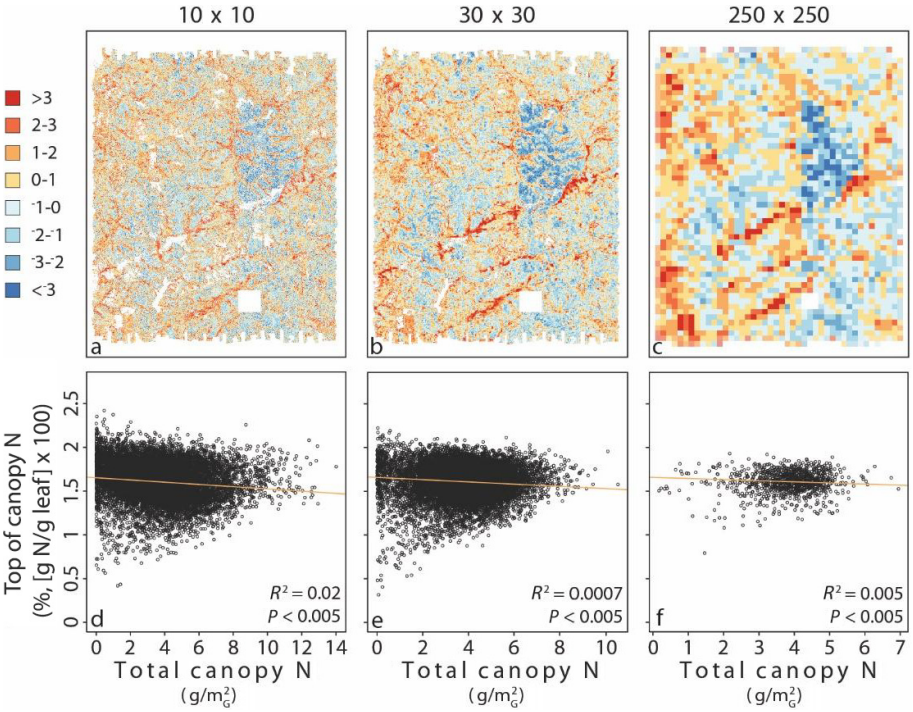

FIG. 5. Maps of the scaled and centered differences between top-of-canopy percent N and total canopy N (g/m_G^2) at three different spatial resolutions: (a) 10 × 10 m (NEON AOP lidar), (b) 30 × 30 m (Landsat), and (c) 250 × 250 m (MODIS). Regression results showing no relationship between the two measurements at (d) 10 x 10 m, (e) 30 x 30 m, and (f) 250 x 250 m. The color key for parts a, b, and c refers to normalized differences between top of canopy percent N and total canopy N.

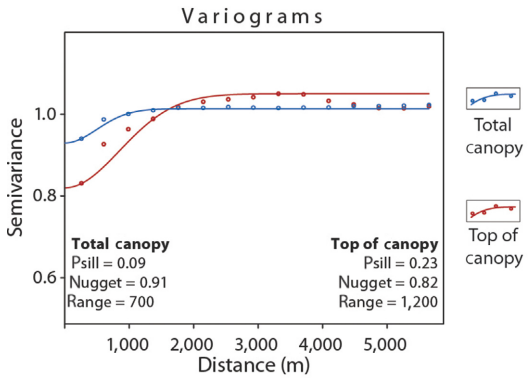

FIG. 6. Variograms for normalized (mean = 0, SD = 1) top-of-canopy percent N (%) and total canopy N (g/m_G^2). A total of 10,000 random samples were extracted from both data sets. Psill, partial sill.

(coefficient > 0.1) with a negative coefficient, while the only major topographic predictor with a positive coefficient was distance from western collection boundary (easting). Alluvial substrate was the only major geologic predictor (coefficient > 0.1) and it had a positive coefficient. There were no major management (coefficient > 0.1) predictors in the total canopy regressions.

For both regression models, many of the management variables appeared in only a small percentage of the total models. This is because these management practices were only completed across a small fraction of the entire landscape, and these areas were not randomly sampled in each iteration of the Monte Carlo simulation.

The residuals of both regression models exhibited some spatial autocorrelation with top-of-canopy percent N having a mean Moran's I of 0.03 with a standard deviation of 0.001 and total canopy N (g/m_G^2) having a mean Moran's I of 0.008 with a standard deviation of 0.0006. While this spatial autocorrelation of the residuals would indicate that there is a trend present that we are not capturing, the aim of these regression was not predictive, but instead to compare the influence of these abiotic and management variables between the two functional traits estimates.

DISCUSSION

We used airborne remote sensing and field-collected trait data to show that when three-dimensional forest structure is considered, different patterns of N appear across this landscape than are produced by two-dimensional top-of-canopy functional trait estimates. This analysis demonstrates that canopy functional diversity is not equivalent to leaf functional diversity, which illustrates the dampened variation in total canopy N between PFTs and across this landscape when compared to the

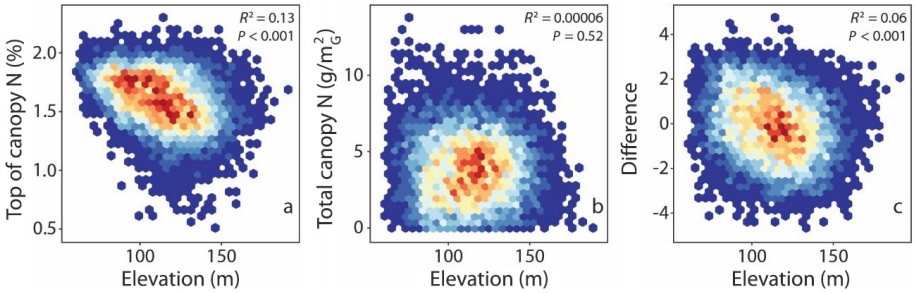

FIG. 7. Heat maps showing the relationship between top-of-canopy percent N (%), total canopy N (g/m$_G^2$), the normalized difference between these two measurements, and elevation.

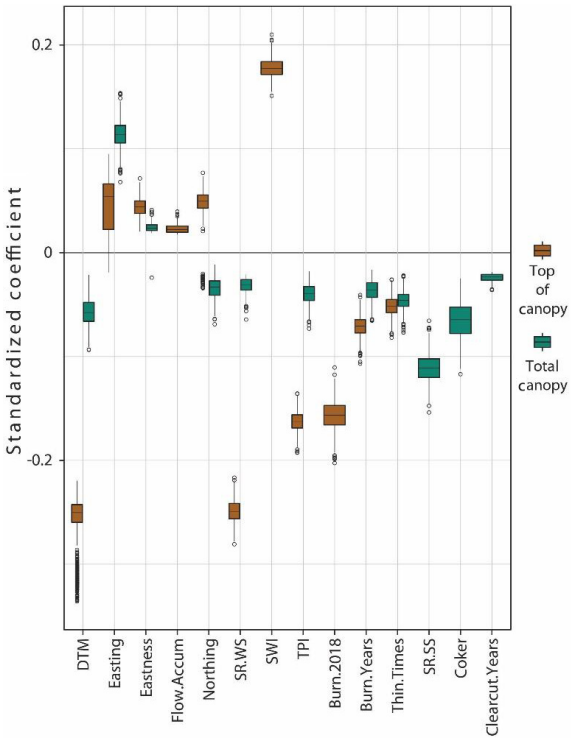

FIG. 8. Coefficients from standardized variables (mean = 0, SD = 0.5) from Monte Carlo simulations with variables that appeared in at least 20% of the regressions. All coefficients have a $P < 0.05$. Box plot components are mid line (median), box edges contain the interquartile range, whiskers refer to the minimum and maximum values excluding outliers, and circles refer to outliers. Variables are refered to in Supplement Table S2 and include (in order from left to right) DTM (elevation), Easting (meters from collection boundary), Eastness (aspect), Flow.Accum (flow accumulation), Northing (meters from collection boundary), SR.WS (solar radiation–winter solstice), SWI (soil wetness index), TPI (topographic position index), Burn.2018 (Areas burned in 2018), Burn.Years (Years since last burn), Thin.Times (Times thinned since 1991), SR.SS (solar radiation–summer solstice), Coker (Coker substrate), Clearcut.Years (Years since last clear cut).

heterogeneous spatial patterns produced by leaf functional diversity. This suggests that these two measurements correspond to different ecological processes and that relationships between plant carbon assimilation and leaf functional traits must be considered in the context of canopy vertical structural heterogeneity.

Scaling and mapping leaf and canopy traits

Many studies have used HSI data to estimate plant functional traits and lidar data to measure forest structure, with much success across a wide variety of ecoregions (Dahlin et al. 2013, Asner et al. 2015, Stark et al. 2015, Smith et al. 2019). By combining 3D structural traits from lidar and 2D functional traits from HSI, we show that a fusion of these two data types can be used to model traits within the canopy volume. Moreover, our findings are within the ranges reported in field-based studies for LAD (Brown and Parker 1994, Parker and Tibbs 2004), percent N (Serbin et al. 2014), LMA (g/m$_L^2$; Poorter et al. 2009), and total canopy N (g/m$_G^2$; Cole and Rapp 1981; Fig. 9).

Our study focuses on an ecoregion consisting of closed-canopy broadleaf stands and sparser needleleaf forests, with our within-canopy trait estimates being reliable across these two plant functional types (PFTs). In addition, our within-canopy model utilizes variables related to the differences in PFTs (top-of-canopy percent N), the local light environment (standard deviation of LAD within a column of voxels), and light capture (euphotic zone depth). These variables have been shown to be critical to canopy-level processes (Field and Mooney 1986, Lefsky et al. 1999, Harding et al. 2001).

While our results show that we can accurately model foliar functional traits within the canopy volume in this ecosystem, more research is needed in different biomes to test the ability of HSI and lidar to accurately estimate within-canopy traits.

Measuring ecosystem function: top-of-canopy percent N vs. total canopy N

While both foliar N and LMA have been identified as key drivers of plant functional diversity (Díaz et al. 2016) and have shown strong correlations with leaf

Table 2. Mean standardized coefficients (mean = 0, SD = 0.5), standard deviation of coefficients, and percentage of models each variable was present from Monte Carlo simulations.

	Top-of-canopy			Total canopy		
Variables	Mean coefficient	Standard deviation	Models present (%)	Mean coefficient	Standard deviation	Models present (%)
Topographic						
DTM	−0.259	0.027	100.0	−0.057	0.013	99.8
Easting	0.047	0.023	30.9	0.114	0.013	100.0
Eastness	0.044	0.009	99.8	0.024	0.005	20.9
Flow accumulation	0.023	0.004	35.3	−0.017	0.018	11.2
Northing	0.047	0.017	85.1	−0.034	0.009	70.0
Northness	NA	NA	0.0	0.027	0.006	4.7
Surface roughness	NA	NA	0.0	NA	NA	0.0
Slope	NA	NA	0.0	NA	NA	0.0
Solar radiation at summer solstice	NA	NA	0.0	−0.111	0.013	100.0
Solar radiation at winter solstice	−0.249	0.011	100.0	−0.032	0.007	44.3
Soil Wetness Index	0.178	0.009	100.0	NA	NA	0.0
Topographic Position Index	−0.162	0.009	100.0	−0.040	0.009	97.1
Topographic Ruggedness Index	NA	NA	0.0	NA	NA	0.0
Geologic substrate						
Alluvial	−0.091	0.151	1.3	0.153	0.158	8.3
Coker	−0.144	0.015	18.1	−0.065	0.017	86.6
Eutaw	0.146	0.013	18.1	0.021	0.036	5.7
Gordo	−0.023	0.008	7.9	0.038	0.009	7.6
Management						
Prescribed burn 2018	−0.157	0.014	100.0	0.034	0.020	3.0
Times burned	NA	NA	0.0	0.025	0.010	7.8
Years since last burn	−0.071	0.010	100.0	−0.036	0.010	90.9
Times chemically treated	−0.009	0.020	4.8	−0.017	0.017	4.3
Years since last chemical treatment	−0.021	0.003	2.1	−0.002	0.023	2.5
Times clearcut	−0.013	0.020	7.5	−0.015	0.019	2.4
Years since last clearcut	−0.023	0.008	17.3	−0.024	0.004	24.6
Times thinned	−0.052	0.009	100.0	−0.046	0.009	98.2
Years since last thinning	NA	NA	0.0	−0.041	0.006	1.8

Note: All coefficients have $P < 0.05$. All variables are referenced in Supplement Table S2.

photosynthesis in temperate ecosystems (Field and Mooney 1986, Evans 1989), we show that the spatial patterns of leaf-level top-of-canopy percent N are not equivalent to those of total canopy N (g/m$_G^2$). Top-of-canopy leaf-level traits reflect key differences between PFTs, with needleleaf species exhibiting low percent N and high LMA, while broadleaf species have higher percent N and lower LMA (Appendix S1: Fig. S1). These fundamental differences in functional and structural traits between PFTs produce distinct dendritic patterns across this landscape corresponding to topographic features including drainages, which are dominated by broadleaf species, and slopes and ridges, which are dominated by pines (Fig. 3a–d). However, when three-dimensional canopy structure is considered (i.e., total canopy N), these distinct landscape patterns are dampened (Fig. 4).

Fig. 7 further shows that these distinct spatial patterns related to elevation are not reflected in our estimates of total canopy N (g/m$_G^2$). This may suggest that canopy architectural differences between PFTs are causing unique distributions of N within the canopies of individual trees (Fig. 4a, b), and that these differences represent trade-offs since different PFTs exhibit similar total quantities of N (g/m$_G^2$) in their canopies (Fig. 9). In this case, differences over a leaf function-structural architecture trade-off produce the dampened spatial patterns we see in this landscape (Fig. 4).

Given the importance of N for photosynthesis, these dampened spatial patterns may not be surprising. By varying LMA, individual trees will distribute N (g/m$_L^2$) throughout their canopies in ways to maximize their nitrogen use efficiency, utilizing as much of the available N (g/m$_G^2$) as possible. Lower total N (g/m$_G^2$) within the canopy volume would imply lower production, a disadvantage that would be hard to reconcile between PFTs in the same ecosystem. While N-fixing trees could change these patterns, we observed no N-fixing trees in this landscape and overall, this area appears to have low N-fixing tree abundance (Staccone et al. 2020).

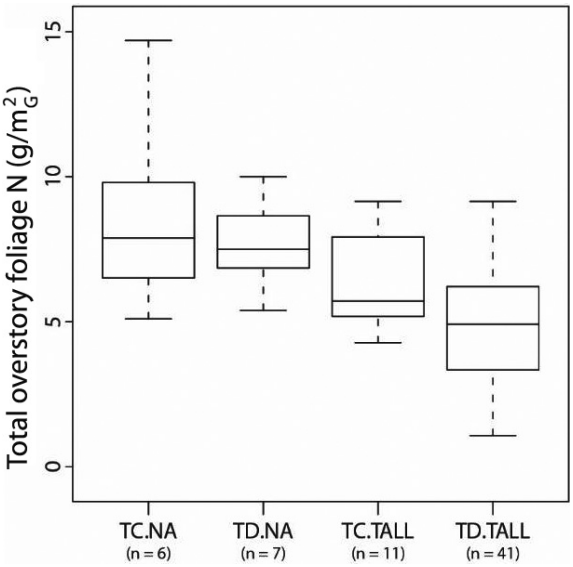

FIG. 9. North American foliar N values vs. Talladega National Forest, Oakmulgee Ranger District (TALL) foliar N values. TC, temperate coniferous; TD, temperate deciduous. North American N (NA) values come from Cole and Rapp (1981). Because our values calculated at TALL do not include the lowest 10 m of the canopy, ANOVA results ($P < 0.001$) show a significant difference between NA and TALL values but not between forest types (TC and TD). Boxplot components are refered to in Fig. 8.

Abiotic and management drivers of foliar and canopy N

Following community assembly theory (Keddy 1992), abiotic drivers have been shown to predict species and leaf trait distributions within landscapes with both remote-sensing and field observations (Kraft et al. 2008, Dahlin et al. 2012). We show that these same types of drivers can be used to predict top-of-canopy percent N in this system, but not total canopy N (g/m$_G^2$).

Top-of-canopy percent N patterns have consistently strong topographic, substrate, and management predictors, with many of these predictors being related to the distribution of PFTs across this landscape. For example, higher elevation areas that receive more solar radiation during the winter months and that were treated with a prescribed burn in 2018 prior to NEON AOP flights had consistently lower top-of-canopy percent N values. This describes the spatial distribution of needleleaf species in this ecosystem. Conversely, lower elevation areas with a high soil water content had consistently higher top-of-canopy percent N values, describing the distribution of broadleaf species in this environment. These relationships suggest that the spatial patterns of top-of-canopy percent N are closely related to the spatial distribution of species within this ecosystem.

In contrast, variables related primarily to forest structural changes and water availability were the main drivers of total canopy N (g/m$_G^2$), even though these relationships were considerably weaker, though still significant. For instance, areas that had been clear-cut, thinned, or burned had lower total canopy N (g/m$_G^2$) estimates than areas that did not have a documented management history. This relationship is most likely due to management activities resulting in significant structural changes to forest stands and the removal of foliar biomass during these activities. Furthermore, areas that received high solar radiation in the summer months also had lower estimates of total canopy N (g/m$_G^2$). This could be due to microclimatic effects. Water stress in these sunnier, drier areas may cause a reduction in growth and, therefore, total canopy N (g/m$_G^2$), as light availability is not likely to be a limiting factor in this system.

Model uncertainty and data concerns

There are many possible sources of error and uncertainty to consider when scaling traits from leaf to landscape, including those related to field and GPS collections, laboratory equipment, remote-sensing sensors, and statistical methodologies. While we did not conduct a formal assessment of uncertainty as it propagates through this study, our findings are within the ranges reported in many field-based studies (see *Scaling and mapping leaf and canopy traits*). Our final PLSR models did show a systematic bias of slightly underestimating N and LMA in needleleaf species (Appendix S1: Figs. S2, S3), which could partially explain the differing landscape-scale relationships between total canopy and top-of-canopy N. This could possibly be improved by the inclusion of forest structure metrics such as LAI in the PLSR models. However, due to the low-density lidar data, we are forced to estimate structural traits at a coarser spatial resolution (10 × 10 m) than the HSI data (1 × 1 m). Because some field samples are closer than 10 m to one another, and thus exist within the same pixel, the inclusion of structural traits did not correct this bias.

While understory shade tolerant plants play an important role in ecosystem functioning (Valladares et al. 2016), we ignored the lowest 10 m of the forest canopy where many of these species occur due to limitations with the lidar data from the NEON AOP (Kamoske et al. 2019). As current lidar sensors within the NEON AOP are upgraded, we will be able to ask important questions about the role of the understory in ecosystem functioning.

In this study, we only considered healthy green forest vegetation, which may partially explain the weaker relationships between environmental variables and canopy functional and structural traits. More research is needed into how HSI and PLSR perform in stressed terrestrial environments and across more heterogeneous landscapes.

The development of a universal model to predict leaf- and canopy-level traits was beyond the scope of this project; however, as more within-canopy foliar traits are

collected across a diversity of ecosystems, PFTs, and tree species, these models will become more robust and can be applied to other regions.

Looking forward

With airborne and spaceborne platforms like the NEON AOP, NASA Goddard's Lidar, Hyperspectral, and Thermal Imager (G-LiHT; Cook et al. 2013), the Global Ecosystem Dynamics Investigation (GEDI; Stavros et al. 2017), and the proposed Surface Biology and Geology Mission (SBG; National Academies of Sciences, Engineering, and Medicine 2018) collecting HSI and lidar data across a variety of ecoregions, there is a unique opportunity for researchers to ask and answer questions related to how forest canopies function across landscapes and continents, rather than just the leaves at the top of the canopy.

In support of these new questions about ecosystem function, we present a reproducible methodology to model foliar traits throughout the entire canopy volume. We also show that the spatial patterns produced by traditional top-of-canopy measurements of percent N are dramatically different than those produced when three-dimensional forest structure is considered. While more research is needed to test these relationships in different ecoregions and across latitudinal gradients, this ever-increasing availability of HSI and lidar data will provide new and exciting opportunities.

These opportunities may raise several questions about the drivers of canopy function, for example, (1) what is the role of soil nutrient availability and heterogeneity in canopy function and (2) how are these relationships affected by latitudinal gradients and climate regimes? Further research is needed into these questions to better understand the drivers behind ecosystem functioning in horizontal and vertical space as well as through time.

Conclusions

Forest structural and functional diversity drive critical canopy processes related to carbon sequestration; however, structure and function are rarely considered in unison at ecosystem scales. Here we show that when forest structure is considered, the patterns produced by the total amount of N (g/m^2) within the canopy volume are substantially different from the patterns produced by top-of-canopy percent N. Furthermore, since total canopy N variation is dampened relative to leaf-level variation over a landscape characterized by variable PFT dominance, we find evidence of canopy architecture and leaf function tradeoffs. Patterns of total N are driven by different abiotic gradients and management regimes, further showing the differences between these two estimates of ecosystem function.

These differing spatial patterns, as well as differing abiotic and management drivers, show that canopy functional diversity is not equivalent to leaf functional diversity. By not considering structure and function together, there could be impacts on how we scale fine-resolution ecological processes to landscape, continental, and global models. However, with new space- and airborne remote sensing platforms collecting HSI and lidar data across a variety of ecoregions, we have an opportunity to think about the terrestrial carbon cycle in three dimensions. This new approach will potentially unlock important insights into how forests function in a time of rapid anthropogenic and environmental change.

Acknowledgments

Thanks to the Talladega National Forest, Oakmulgee Ranger District for providing site access, to NEON staff for providing technical support, and to O. Jain for providing assistance in the field. This work was supported in part by the NSF Macrosystem Biology Program award #1702379. The NEON is a program sponsored by the National Science Foundation and operated under cooperative agreement by Battelle Memorial Institute. This material is based in part upon work supported by the National Science Foundation through the NEON Program. Shawn P. Serbin was partially supported by the United States Department of Energy contract No. DE-SC0012704 to Brookhaven National Laboratory.

Literature Cited

Asner, G. P., C. Anderson, R. E. Martin, D. E. Knapp, R. Tupayachi, and T. Kennedy-Bowdoin. 2014. Landscape-scale changes in forest structure and functional traits along an Andes-to-Amazon elevation gradient. Biogeosciences 11:843–856.

Asner, G. P., and R. E. Martin. 2009. Airborne spectranomics: mapping canopy chemical and taxonomic diversity in tropical forests. Frontiers in Ecology and Environment 7:269–276.

Asner, G. P., R. E. Martin, C. B. Anderson, and D. E. Knapp. 2015. Quantifying forest canopy traits: imaging spectroscopy versus field survey. Remote Sensing of Environment 158:15–27.

Atkins, J. W., R. T. Fahey, B. H. Hardiman, and C. M. Gough. 2018. Forest canopy structural complexity and light absorption relationships at the subcontinental scale. Journal of Geophysical Research: Biogeosciences 123:1387–1405.

Bachofen, C., P. D'Odorico, and N. Buchmann. 2020. Light and VPD gradients drive foliar nitrogen partitioning and photosynthesis in the canopy of European beech and silver fir. Oecologia 192:323–339.

Bater, C. W., and N. C. Coops. 2009. Evaluation error associated with lidar-derived DEM interpolation. Computers & Geosciences 35:289–300.

Brown, M. J., and G. G. Parker. 1994. Canopy light transmittance in a chronosequence of mixed-species deciduous forests. Canadian Journal of Forest Research 24:1694–1703.

Burnham, K. P., D. R. Anderson, and K. P. Huyvaert. 2011. AIC model selection and multimodel inference in behavioral ecology: some background, observations, and comparisons. Behavioral Ecology and Sociobiology 65:23–35.

Chambers, J. Q., G. P. Asner, D. C. Morton, L. O. Anderson, S. S. Saatchi, F. D. B. Espirito-Santo, M. Palace, and C. Souza Jr. 2007. Regional ecosystem structure and function: ecological insights from remote sensing of tropical forests. Trends in Ecology & Evolution 22:414–423.

Clark, M. L., D. A. Roberts, and D. B. Clark. 2005. Hyperspectral discrimination of tropical rain forest tree species at leaf to crown scales. Remote Sensing of Environment 96:375–398.

Cole, D. W., and M. Rapp. 1981. Elemental cycling in forest ecosystems. Pages 341–409 *in* D. E. Reichle, editor. Dynamic

properties of forest ecosystems. Cambridge University Press, Cambridge, UK.

Colgan, M. S., C. A. Baldeck, J.-B. Féret, and G. P. Asner. 2012. Mapping savanna tree species at ecosystem scales using support vector machine classification and BRDF correction on airborne hyperspectral and LiDAR data. Remote Sensing 4:3462–3480.

Collings, S., P. Caccetta, N. Campbell, and X. Wu. 2010. Techniques for BRDF correction of hyperspectral mosaics. IEEE Transactions on Geoscience and Remote Sensing 48:3733–3746.

Cook, B. D., L. A. Corp, R. F. Nelson, E. M. Middleton, D. C. Morton, J. T. McCorkel, J. G. Masek, K. J. Ranson, V. Ly, and P. M. Montesano. 2013. NASA Goddard's LiDAR, hyperspectral and thermal (G-LiHT) airborne imager. Remote Sensing 5:4045–4066.

Dahlin, K. M., G. P. Asner, and C. B. Field. 2012. Environmental filtering and land-use history drive patterns in biomass accumulation in a Mediterranean-type landscape. Ecological Applications 22:104–118.

Dahlin, K. M., G. P. Asner, and C. B. Field. 2013. Environmental and community controls on plant canopy chemistry in a Mediterranean-type ecosystem. Proceedings of the National Academy of Sciences USA 110:6895–6900.

Dahlin, K. M., G. P. Asner, and C. B. Field. 2014. Linking vegetation patterns to environmental gradients and human impacts in a Mediterranean-type island ecosystem. Landscape Ecology 29:1571–1585.

Dandois, J. P., and E. C. Ellis. 2013. High spatial resolution three-dimensional mapping of vegetation spectral dynamics using computer vision. Remote Sensing of Environment 136:259–276.

Díaz, S., et al. 2016. The global spectrum of plant form and function. Nature 529:167–171.

Ellsworth, D. S., and P. B. Reich. 1993. Canopy structure and vertical patterns of photosynthesis and related leaf traits in a deciduous forest. Oecologia 96:169–178.

Evans, J. R. 1989. Photosynthesis and nitrogen relationship in leaves of C3 plants. Oecologia 78:9–19.

Fahey, R. T., A. T. Fotis, and K. D. Woods. 2015. Quantifying canopy complexity and effects on productivity and resilience in late-successional hemlock-hardwood forests. Ecological Applications 25:834–847.

Field, C. B., and H. A. Mooney. 1986. The photosynthesis-nitrogen relationship in wild plants. Pages 25–56 *in* T. J. Givnish, editor. On the economy of plant form and function. Cambridge University Press, Cambridge, UK.

Gelman, A. 2007. Scaling regression inputs by dividing by two standard deviations. Statistics in Medicine 27:2865–2873.

Gougeon, F. A. 1995. Comparison of possible multispectral classification schemes for tree crowns individually delineated on high spatial resolution MEIS images. Canadian Journal of Remote Sensing 21:1–9.

Gough, C. M., J. W. Atkins, R. T. Fahey, and B. S. Hardiman. 2019. High rates of primary production in structurally complex forests. Ecology 100:e02864.

Hardiman, B. S., G. Bohrer, C. M. Gough, C. S. Vogel, P. S. Curtis, S. Vogel, S. Curtis, and S. Hardiman. 2011. The role of canopy structural complexity in wood net primary production of a maturing northern deciduous forest. Ecology 92:1818–1827.

Hardiman, B. S., C. M. Gough, A. Halperin, K. L. Hofmeister, L. E. Nave, G. Bohrer, and P. S. Curtis. 2013. Maintaining high rates of carbon storage in old forests: a mechanism linking canopy structure to forest function. Forest Ecology and Management 298:111–119.

Harding, D. J., M. A. Lefsky, G. G. Parker, and J. B. Blair. 2001. Laser altimeter canopy profiles methods and validation for closed-canopy, broadleaf forests. Remote Sensing of Environment 76:283–297.

Hijmans, R. J. 2019. raster: geographic data analysis and modeling. R package version 2.9-5. https://cran.r-project.org/web/packages/raster/index.html

Horton, J. D., C. A. San Juan, and D. B. Stoeser. 2017. The State Geologic Map Compilation (SGMC) geodatabase of the conterminous United States (ver. 1.1, August 2017): U.S. Geological Survey Data Series 1052, 46 p. https://doi.org/10.3133/ds1052

Iglhaut, J., C. Cabo, S. Puliti, L. Piermattei, J. O'Connor, and J. Rosette. 2019. Structure from motion photogrammetry in forestry: a review. Current Forestry Reports 5:155–168.

Kamoske, A. G., K. M. Dahlin, S. C. Stark, and S. P. Serbin. 2019. Leaf area density from airborne LiDAR: comparing sensors and resolutions in a temperate broadleaf forest ecosystem. Forest Ecology and Management 433:364–375.

Kampe, T. U., B. R. Johnson, M. Kuester, and M. Keller. 2010. NEON: the first continental-scale ecological observatory with airborne remote sensing of vegetation canopy biochemistry and structure. Journal of Applied Remote Sensing 4:043510.

Keddy, P. A. 1992. Assembly and response rules: two goals for predictive community ecology. Journal of Vegetation Science 3:157–164.

Kraft, N. J. B., R. Valencia, and D. D. Ackerly. 2008. Functional traits and niche-based tree community assembly in an Amazonian forest. Science 322:580–582.

Leblanc, S. G., J. M. Chen, R. Fernandes, D. W. Deering, and A. Conley. 2005. Methodology comparison for canopy structure parameters extraction from digital hemispherical photography in boreal forests. Agricultural and Forest Meteorology 129:187–207.

Lefsky, M. A., W. B. Cohen, S. A. Acker, G. G. Parker, T. A. Spies, and D. Harding. 1999. Lidar remote sensing of the canopy structure and biophysical properties of Douglas-fir Western Hemlock forests. Remote Sensing of Environment 70:339–361.

MacArthur, R. H., and H. S. Horn. 1969. Foliage profile by vertical measurements. Ecology 50:802–804.

Martens, H., and M. Martens. 2000. Modifiend Jack-knife estimation of parameter uncertainty in bilinear modelling by partial least squares regression (PLSR). Food Quality and Preference 5:1–16.

Mascaro, J., G. P. Asner, H. C. Muller-Landau, M. Van Breugel, J. Hall, and K. Dahlin. 2011. Controls over aboveground forest carbon density on Barro Colorado Island, Panama. Biogeosciences 8:1615–1629.

Mevik, B., and R. Wehrens. 2007. The pls package: principal component and partial least squares regression in R. Journal of Statistical Software 18:1–23.

National Academics of Sciences, Engineering, and Medicine. 2018. Thriving on our changing planet: a decadal strategy 650 for Earth observation from space. National Academies Press, Washington, D.C., USA.

Niinemets, Ü. 2007. Photosynthesis and resource distribution through plant canopies. Plant, Cell and Environment 30:1052–1071.

Niinemets, Ü. 2012. Optimization of foliage photosynthetic capacity in tree canopies: towards identifying missing constraints. Tree Physiology 32:505–509.

Niinemets, Ü., T. F. Keenan, and L. Hallik. 2015. A worldwide analysis of within-canopy variations in leaf structural, chemical and physiological traits across plant functional types. New Phytologist 205:973–993.

Ollinger, A. S. V., M. L. Smith, M. E. Martin, R. A. Hallett, C. L. Goodale, and J. D. Aber. 2002. Regional variation in foliar chemistry and N cycling among forests of diverse history and composition. Ecology 83:339–355.

Parker, G. G., M. E. Harmon, M. A. Lefsky, J. Chen, R. Van Pelt, S. B. Weiss, S. C. Thomas, W. E. Winner, D. C. Shaw,

and J. F. Franklin. 2004. Three-dimensional structure of an old-growth Pseudotsuga-tsuga canopy and its implications for radiation balance, microclimate, and gas exchange. Ecosystems 7:440–453.

Parker, G. G., and D. J. Tibbs. 2004. Structural phenology of the leaf community in the canopy of a *Liriodendron tulipifera* L. forest in Maryland, USA. Forest Science 50:387–397.

Pedro, M. S., W. Rammer, and R. Seidl. 2017. Disentangling the effects of compositional and structural diversity on forest productivity. Journal of Vegetation Science 28:649–658.

Pisek, J., et al. 2018. Data synergy between leaf area index and clumping index Earth Observation production using photon recollision probability theory. Remote Sensing of Environment 215:1–6.

Poorter, H., Ü. Niinemets, L. Poorter, I. J. Wright, and R. Villar. 2009. Causes and consequences of variation in leaf mass per area (LMA): a meta-analysis. New Phytologist 182:565–588.

Reich, P. B., M. B. Walters, and D. S. Ellsworth. 1997. From tropics to tundra: Global convergence in plant functioning. Proceedings of the National Academy of Sciences USA 94:13730–13734.

Richardson, J. J., L. M. Moskal, and S. H. Kim. 2009. Modeling approaches to estimate effective leaf area index from aerial discrete-return LIDAR. Agricultural and Forest Meteorology 149:1152–1160.

Running, S. W., R. R. Nemani, F. A. Heinsch, M. Zhao, M. Reeves, and H. Hashimoto. 2004. A continuous satellite-derived measure of global terrestrial primary production. BioScience 54:547.

Sabol, J., Z. Patočka, and T. Mikita. 2014. Usage of Lidar data for leaf area index estimation. GeoScience Engineering 60:10–18.

Scheuermann, C. M., L. E. Nave, R. T. Fahey, K. J. Nadelhoffer, and C. M. Gough. 2018. Effects of canopy structure and species diversity on primary production in upper Great Lakes forests. Oecologia 188:405–415.

Schimel, D. S. 1995. Terrestrial biogeochemical cycles: global estimates with remote sensing. Remote Sensing of Environment 51:49–56.

Schimel, D., R. Pavlick, J. B. Fisher, G. P. Asner, S. Saatchi, P. Townsend, C. Miller, C. Frankenberg, K. Hibbard, and P. Cox. 2015. Observing terrestrial ecosystems and the carbon cycle from space. Global Change Biology 21:1762–1776.

Schimel, D., F. D. Schneider, and JPL Carbon and Ecosystem Participants. 2019. Flux towers in the sky: global ecology from space. New Phytologist 224:570–584.

Schlapfer, D., R. Richter, and T. Feingersh. 2015. Operational BRDF effects correction for wide-field-of-view optical scanners (BREFCOR). IEEE Transactions on Geoscience and Remote Sensing 53:1855–1864.

Schneider, C. A., W. S. Rasband, and K. W. Eliceiri. 2012. NIH Image to ImageJ: 25 years of image analysis. Nature Methods 9:671–675.

Serbin, S. P., A. Singh, B. E. McNeil, C. C. Kingdon, and P. A. Townsend. 2014. Spectroscopic determination of leaf morphological and biochemical traits for northern temperate and boreal tree species. Ecological Applications 24:1651–1669.

Shao, G., S. C. Stark, D. R. A. de Almeida, and M. N. Smith. 2019. Towards high throughput assessment of canopy dynamics: the estimation of leaf area structure in Amazonian forests with multitemporal multi-sensor airborne lidar. Remote Sensing of Environment 221:1–13.

Shi, Y., T. Wang, A. K. Skidmore, and M. Heurich. 2018. Important LiDAR metrics for discriminating forest tree species in Central Europe. ISPRS Journal of Photogrammetry and Remote Sensing 137:163–174.

Singh, A., S. P. Serbin, B. E. McNeil, C. C. Kingdon, and P. A. Townsend. 2015. Imaging spectroscopy algorithms for mapping canopy foliar chemical and morphological traits and their uncertainties. Ecological Applications 25:2180–2197.

Smith, M. N., et al. 2019. Seasonal and drought-related changes in leaf area profiles depend on height and light environment in an Amazon forest. New Phytologist 222:1284–1297.

Soenen, S. A., D. R. Peddle, and C. A. Coburn. 2005. SCS+C: a modified Sun-canopy-sensor topographic correction in forested terrain. IEEE Transactions on Geoscience and Remote Sensing 43:2148–2159.

Solberg, S., E. Næsset, K. H. Hanssen, and E. Christiansen. 2006. Mapping defoliation during a severe insect attack on Scots pine using airborne laser scanning. Remote Sensing of Environment 102:364–376.

Staccone, A., W. Liao, S. Perakis, J. Compton, C. Clark, and D. Menge. A spatially explicit, empirical estimate of tree-based biological nitrogen fixation in forests of the United States. Global Biogeochemical Cycles 34:1–18.

Stark, S. C., et al. 2012. Amazon forest carbon dynamics predicted by profiles of canopy leaf area and light environment. Ecology Letters 15:1406–1414.

Stark, S. C., B. J. Enquist, S. R. Saleska, V. Leitold, J. Schietti, M. Longo, L. F. Alves, P. B. Camargo, and R. C. Oliveira. 2015. Linking canopy leaf area and light environments with tree size distributions to explain Amazon forest demography. Ecology Letters 18:636–645.

Stavros, E. N., et al. 2017. ISS observations offer insights into plant function. Nature Ecology and Evolution 1:1–4.

Sumida, A., T. Nakai, M. Yamada, K. Ono, S. Uemura, and T. Hara. 2009. Ground-based estimation of leaf area index and vertical distribution of leaf area density in a *Betula ermanii* forest. Silva Fennica 43:799–816.

Townsend, P. A., J. R. Foster, R. A. Chastian Jr., and W. S. Currie. 2003. Canopy nitrogen in the forests of the Central Appalachian Mountains using Hyperion and AVIRIS. IEEE Transactions on Geoscience and Remote Sensing 41:1347–1354.

Tucker, C. J., and P. J. Sellers. 1986. Satellite remote sensing of primary production. International Journal of Remote Sensing 7:1395–1416.

USDA Forest Service. 2005. Longleaf ecosystem-restoration project: final environmental impact statement, National Forests in Alabama. Talladega National Forest, Oakmulgee District, USDA Forest Service, Brent, Alabama, USA.

Valladares, F., L. Laanisto, Ü. Niinemets, and M. A. Zavala. 2016. Shedding light on shade: ecological perspectives of understorey plant life. Plant Ecology and Diversity 9:237–251.

Wanner, W., X. Li, and A. H. Strahler. 1995. On the derivation of kernels for kernel-driven models of bidirectional reflectance. Journal of Geophysical Research 100:21077.

Weiss, M., F. Baret, G. J. Smith, I. Jonckheere, and P. Coppin. 2004. Review of methods for in situ leaf area index (LAI) determination Part II. Estimation of LAI, errors and sampling. Agricultural and Forest Meteorology 121:37–53.

Weyermann, J., M. Kneubühler, D. Schläpfer, and M. E. Schaepman. 2015. Minimizing reflectance anisotropy effects in airborne spectroscopy data using Ross-Li model inversion with continuous field land cover stratification. IEEE Transactions on Geoscience and Remote Sensing 53:5814–5823.

Wright, I. J., et al. 2004. The worldwide leaf economics spectrum. Nature 428:821–827.

Zhao, K., and S. Popescu. 2009. Lidar-based mapping of leaf area index and its use for validating GLOBCARBON satellite LAI product in a temperate forest of the southern USA. Remote Sensing of Environment 113:1628–1645.

Supporting Information

Additional supporting information may be found online at: http://onlinelibrary.wiley.com/doi/10.1002/eap.2230/full

Data Availability

NEON AOP provisional discrete return lidar point clouds (e.g., NEON.DP1.30006.001) and hyperspectral orthorectified surface directional reflectance (e.g., NEON.DP1.30003.001) were downloaded on 4 April 2019 from http://data.neonscience.org. R package to estimate structural traits from airborne LiDAR data is provided on Zenodo at http://doi.org/10.5281/zenodo.3987340. R package to pre-process HSI data, extract reflectance data, and apply PLSR coefficients is provided on Zenodo at http://doi.org/10.5281/zenodo.3987336. Reflectance spectra and trait data are available through the ECOSIS database at: https://data.ecosis.org/dataset/2018-talladega-national-forest--leaf-level-reflectance-spectra-and-foliar-traits. Laboratory measured trait data are available through the TRY Database under data set ID 714.